Title

Gold nanoparticle-mediated photothermal therapy guidance with multi-wavelength photomagnetic imaging

Authors

Nouizi, Farouk
Algarawi, Maha
Erkol, Hakan
et al.

Publication Date

2024-02-01

DOI

10.1016/j.pdpdt.2023.103956

Published in final edited form as:
Photodiagnosis Photodyn Ther. 2024 February ; 45: 103956. doi:10.1016/j.pdpdt.2023.103956.

Gold nanoparticle-mediated photothermal therapy guidance with multi-wavelength photomagnetic imaging

Farouk Nouizi[a], **Maha Algarawi**[b], **Hakan Erkol**[c], **Gultekin Gulsen**[a,*]

[a]Department of Radiological Sciences, University of California Irvine, USA

[b]Department of Physics, Imam Mohammad Ibn Saud Islamic University (IMSIU), Saudi Arabia

[c]Department of Physics, Bogazici University, Turkey

Abstract

Difficulty in heating tumors with high spatial selectivity while protecting surrounding healthy tissues from thermal harm is a challenge for cancer photothermal treatment (PTT). To mitigate this problem, PTT mediated by photothermal agents (PTAs) has been established as a potential therapeutic technique to boost selectivity and reduce damage to surrounding healthy tissues. Various gold nanoparticles (AuNP) have been effectively utilized as PTAs, mainly using strategies to target cancerous tissue and increase selective thermal damage. Meanwhile, imaging can be used in tandem to monitor the AuNP distribution and guide the PTT. Mainly, the parameters impacting the induced temperature can be determined using simulation tools before treatment for effective PTT. However, accurate simulations can only be performed if the amount of AuNPs accumulated in the tumor is known. This study introduces Photo-Magnetic Imaging (PMI), which can appropriately recover the AuNP concentration to guide the PTT. Using multi-wavelength measurements, PMI can provide AuNP concentration based on their distinct absorption spectra. Tissue-simulating phantom studies are conducted to demonstrate the potential of PMI in recovering AuNP concentration for PTT planning. The recovered AuNP concentration is used to model the temperature increase accurately in a small inclusion representing tumor using a multiphysics solver that takes into account the light propagation and heat diffusion in turbid media.

Keywords

Photo-magnetic imaging; Photothermal therapy; Photothermal agents; Gold nanoparticles; Multi-wavelength imaging; Magnetic resonance thermometry

---

[*]Corresponding author. ggulsen@uci.edu (G. Gulsen).

Declaration of Competing Interest
The authors report no declarations of interest.

CRediT authorship contribution statement
Farouk Nouizi: Writing - review & editing, Validation, Software, Project administration, Investigation, Formal analysis, Data curation. **Maha Algarawi:** Writing - review & editing, Visualization, Methodology, Investigation, Data curation. **Hakan Erkol:** Writing - review & editing, Software, Methodology, Investigation, Formal analysis. **Gultekin Gulsen:** Writing - review & editing, Writing - original draft, Supervision, Project administration, Methodology, Conceptualization.

1. Introduction

Local hyperthermia is using heat to treat malignant tumors by elevating the temperature of the entire body and/or local tumor tissue. It can be used alone or in combination with other therapies like radiation, chemotherapy, and immunotherapy in clinical practice. Local hyperthermia is frequently utilized for cervical lymph node metastases and skin tumors [1]. Mild hyperthermia, acute hyperthermia, and tissue coagulation or ablation are all examples of hyperthermia. Mild hyperthermia involves heating the tissue to bring the local temperature in a range of 39 °C to 43 °C. It is commonly used as an adjuvant therapy with radiation or chemotherapy because it makes cells more vulnerable to ionizing radiation therapy or chemotherapy medications [2]. Acute hyperthermia, exposing the tissue to elevated temperatures between 43 °C and 48 °C, can cause reversible harm and malfunction as well as irreversible damage, resulting in either immediate or planned cell death. On the other hand, tissue ablation and coagulation therapy have been linked to significantly greater temperatures than 49 °C.

Photothermal treatment (PTT) is an emerging method of achieving hyperthermia by converting light into heat to kill cancer cells selectively. Because of its straightforward procedure, short treatment period, and rapid recovery, PTT has a high research value [3]. More importantly, PTT is a highly successful and noninvasive cancer treatment that can eradicate a variety of cancers. A primary disadvantage of PTT in cancer treatment is its lack of spatial selectivity in heating tumors while preserving surrounding healthy tissues from thermal injury. To increase selectivity and reduce collateral damage, PTT mediated by photothermal agents (PTAs) has been developed as a viable therapeutic strategy in cancer treatment, overcoming the limits of existing hyperthermia approaches [4].

Due to their biocompatible and plasmonic properties, gold nanoparticles (AuNPs) are widely used as PTAs. AuNPs have plasmon resonance tunability, high photothermal conversion efficiency, and the ability to functionalize their surface. Another advantage of AuNPs is their ability to produce reactive oxygen species [5]. As a result, employing AuNPs in PTT has a synergistic effect on cancer cell destruction. One of the most critical parameters of the AuNPs is the photothermal conversion efficiency parameter, which depends on the size, shape, and local concentration of the AuNPs [6–9]. Since they can be very toxic for cells at high concentrations, optimization of the photothermal conversion efficiency of AuNPs is essential [10]. To predict their conversion efficiency and hence, the local temperature increase during PTT, monodispersity of the injected AuNPs is critical. However, this is one of the most significant challenges during their synthesis [11, 12].

Indeed, the efficiency of the PTT strongly depends on the photothermal conversion efficiency of AuNPs and their concentration in the tumor. Meanwhile, the tumor uptake depends on the local perfusion and injection route as well as the size and shape of the AuNPs. Therefore, it is very challenging to estimate the temperature elevation of a tumor during PTT, even though the laser parameters and photothermal conversion efficiency of the AuNPs are very well known. Imaging can be used in tandem to quantify the concentration of AuNPs to plan the PT procedure for a successful implementation [13]. Due to their high atomic number and capacity to absorb X-rays, AuNPs can also be used for imaging in addition to being attractive candidates for tumor radio-sensitization [14].

Unfortunately, the sensitivity of conventional X-ray CT imaging is low to detect the small amount of AuNPs accumulated in the tumor. However, X-ray fluorescence imaging has been shown to have enough sensitivity to map the distribution of AuNPs. For example, a tumor tagged with AuNPs in a mouse model is undetected by CT, whereas X-ray fluorescence imaging can clearly spot it [15,16]. The main reason for this difference in detection sensitivity is that the contrast in CT is due to the difference in photon counts in the forward (transmission) direction, while fluorescence photons are emitted isotropically, and the detection limit of X-ray fluorescence imaging is determined only by the spectral background in the signal region governed by multiple Compton scattering [17]. Nevertheless, the CT images can provide valuable anatomic information to fuse the X-ray fluorescence functional imaging in living mice. Furthermore, time-lapse images can be acquired to determine the pharmacokinetics of the AuNPs [18].

Alternatively, magnetic resonance imaging (MRI) can be used when AuNPs are loaded with paramagnetic metal complexes such as gadolinium [19,20] or are combined with superparamagnetic materials such as Fe304 particles [21]. More sensitive molecular imaging techniques have also been employed for imaging AuNP-based nanoprobes [22]. Surface-enhanced Raman scattering (SERS) [23], darkfield microscopy (DFM), and optical coherence tomography (OCT) are all among those molecular imaging alternatives [24]. However, imaging depth is limited to superficial tissues in all these techniques.

For whole-body small animal imaging, fluorescence molecular tomography can be used as a molecular imaging modality. For this purpose, AuNPs can be conjugated with fluorescent dyes to take advantage of the distance-dependent quenching of fluorescence signals and create activable probes [25]. Additionally, intrinsically fluorescent gold nanoclusters have been utilized as contrast agents in fluorescence imaging [26–28]. Despite its superior sensitivity, the spatial resolution of fluorescence imaging is unfortunately hampered by the highly scattering nature of the tissue. To overcome this disadvantage, Photoacoustic imaging (PAI) has been developed by combining the high resolution of ultrasound with the high sensitivity of diffuse optical imaging [29,30]. Due to its tunable plasmonic absorbance that can reach the near-infrared region where tissue absorption is low, gold nanorods, gold nanoclusters, and other AuNP-based nanostructures have recently attracted increasing interest for use as contrast agents in PAI [22,31,32].

We have recently developed a first-of-its-kind imaging technique that combines the sensitivity of optical molecular imaging with the high resolution of MRI and termed “Photo-magnetic Imaging (PMI)” [33,34]. In this technique, the temperature maps are acquired in a dynamic fashion with MRI, while the tissue is illuminated with laser light. By modeling propagation of light and diffusion of heat in the tissue, the main idea is to recover the optical properties of the tissue from the measured increase in temperature maps. The problem in conventional optical molecular imaging is that the accuracy of the recovered parameters highly depends on depth, i.e. the accuracy drastically degrades with depth. PMI results are depth-independent as long as the MR measurements are above the noise level. That is the strength of the PMI technique, which is due to the spatially-resolved nature of MR temperature measurements as opposed to the limited boundary measurements obtained in conventional optical molecular imaging. We have previously demonstrated how PMI can guide the PTT using our prototype four-wavelength system designed to recover endogenous tissue contrast [35]. Our prototype system is expanded for imaging exogenous contrast agents such as PTAs in this work. The absorption spectrum of exogenous agents is distinctly different compared to the endogenous chromophores such as water, fat, oxy- and deoxy-hemoglobin. These endogenous chromophores already differ from one another in terms of spectral shape in their absorption spectra [36,37]. As seen in our earlier research, this made it possible for PMI to restore the tissue chromophore concentrations. If PMI measurements are carried out using additional wavelengths, the concentration of the AuNPs can be retrieved because their absorption spectra are also noticeably different. In order to update the PMI system, one additional laser is added in this study, increasing the total number of wavelengths to five. Several tissue-simulating phantoms are prepared by adding AuNPs into the background or small compartments representing tumors. The performance of the PMI in recovering the concentration of the AuNPs and estimating the temperature elevation using a multiphysics solver are successfully investigated.

2. Materials and methods

2.1. PMI instrumentation

The PMI technique has been developed in our lab. It is a novel attempt to make optical and MR systems interact with each other to use their exclusive properties. Unique contrast of optical imaging is used together with high-resolution temperature measurement ability of the MRI, to recover the optical properties of the tissues. PMI uses near-infrared light to heat the tissue only for a couple of degrees and utilizes MRI to measure the 3D temperature distribution with high resolution. The MR temperature maps are further used to calculate the optical properties of the medium under investigation using proper modeling of light propagation and heat transfer in tissue. Using multiple wavelengths, tissue endogenous chromophore concentration namely oxy- and deoxy-hemoglobin, water, and fat can be revealed. Furthermore, multi-wavelength measurements can be further used to estimate the concentration of the PTAs.

To achieve this aim, the upgraded multi-wavelength PMI system utilizes five lasers: 760 nm, 790 nm, 808 nm, 860 nm, and 980 nm. Fig. 1 a shows a picture of the portable PMI system that consists of high-power lasers and their drivers, a temperature management system, and a control computer. Besides this portable unit, the second counterpart of the PMI is a fiber bundle coupled RF-coil for obtaining MR temperature maps, Fig. 1 b. PMI is a simple add-on to the MRI with these two units due to its non-complex instrumentation since no optical detection system is required. The output power for each laser is measured by a power meter (PMI0–10, Thorlabs Inc.) before the experiments for calibration purposes. Considering that the output power is set to 1.5 W and the 1.3 cm diameter laser spot on the phantom, the maximum power density at the surface of the phantom is 1.13 W.cm^{-2}.

PMI non-invasively monitors the temperature evolution inside the volume under investigation using magnetic resonance thermometry (MRT) [38–40]. MRT provides high-resolution temperature maps that are used to calculate the optical absorption coefficient of the medium. For this purpose, an RF-coil is utilized with an opening on top, which is used as a port for laser illumination. An optical fiber bundle is custom-built in our lab to transfer the laser outputs from the central PMI unit located in the MR control room to the RF-coil via the tubular waveguides in the penetration panel, Fig. 2.a. The bundle has seven 1-mm diameter optical fibers, each connected to the output of a different laser. At the other end, a collimation lens (35 mm; Newport Corporation, Irvine, CA, US) is used to collimate the light and have a uniform illumination at the phantom surface as seen in Fig. 2.b.

A LabVIEW program is implemented to control all the operating functionalities automatically. These include monitoring and adjusting the laser current, measuring laser temperatures, and controlling the thermoelectric laser cooling units and fans. During PMI data acquisition, MRT temperature maps are acquired dynamically. First, baseline MRT images are acquired for a particular wavelength. Following that, the laser is turned on while temperature maps are continuously acquired for this heating phase. Once this phase is completed, the laser is turned off, while temperature maps are still being acquired till this cooling phase ends, Fig. 3.

2.2. Preparation of phantoms

Gelatin phantoms are the method of choice for this study since the turbidity and optical absorption of high-purity agarose gels are relatively low. As a result, the optical properties of agarose-based phantoms might be simply constructed with suitable light scattering and absorption agents [41]. More importantly, they allow the creation of compartments and the mixing AuNPs in desired amounts [42]. The phantoms are all cylindrical with a diameter of 25 mm. India ink (Color Code:1,111,030, Winsor & Newton Ltd.) is utilized as a dye to adjust the absorption coefficient. First, a stock solution is prepared by dissolving 60 mg of Indian Ink in 5.3 L of distilled water. During phantom preparation, 0.35 ml of this stock solution is added to a total of 100 ml of the final solution with all other ingredients, including agarose gel. Hence, the dye concentration in the phantom material is about 39.6 ng/ml.

The absorption of Indian Ink at this concentration is measured by a commercial spectrometer (USB2000, Ocean Optics Inc., USA) in our lab. It changes very little in the wavelength range of 760 nm to 860 nm, from 0.0101 mm^{-1} down to 0.0097 mm^{-1}, as seen in Table 1. Meanwhile, Intralipid® 20 % (Fresenius Kabi Inc.) is added to the phantoms to bring the reduced scattering coefficient to 0.86 mm^{-1} at 800 nm. The absorption and the reduced scattering coefficients of the phantom are confirmed with Diffuse Optical Tomography system developed in our lab [43–45]. These measurements also reveal the contribution of fat and water, as presented in Table 1.

Three different phantoms are constructed for this study. The first phantom is homogenous, containing only Indian ink as an absorber (Homogeneous Dye). The second phantom has the same properties, but AuNPs nanorods are added to the solution to increase the overall absorption (Homogeneous AuNPs). The nanorods are 10 nm in diameter with a peak absorption of around 850 nm (A12–10-808, Nanopartz, Inc.). The concentration of the stock AuNPs solution synthesized by the company is 0.042 mg/ml. Some of this stock solution is used to make the phantom, in which the concentration of AuNPs is approximately 7.33 Hg/ml. The absorption coefficient of this AuNPs concentration is 0.0267 mm^{-1}, nearly three times the Indian ink absorption at 860 nm. Our spectrometer measurements show that their absorption is less at the lower wavelengths, particularly at 790 and 760 nm as expected, Table 1. Therefore, there is a distinct difference in the wavelength-dependent absorption patterns of the India ink and AuNPs nanorods that allows distinguishing their presence utilizing multi-wavelength measurements.

These two homogeneous phantoms are mainly used to verify the PMI system's ability to distinguish the Indian Ink and AuNPs concentrations. The total absorption of each phantom calculated by adding all components is given in Table 1. Following that, a third heterogeneous phantom, having only Indian Ink in the background and a small compartment representing a tumor composed of both Indian Ink and AuNPs, is constructed. This inclusion is 8.8 mm in diameter and placed 1.9 mm below the upper surface. The background and the inclusion of this phantom have the very same composition with homogeneous Dye and homogeneous AuNP phantoms, respectively. The T1-weighted anatomic MR images of the phantoms are presented in Fig. 4. Please note that the inclusion is also made from agar so that the phantom has no discontinuity regarding light and heat diffusion. Since more than 90 % of this phantom is water, the thermal properties were the same as water values. The water density, specific heat, and heat conductivity values are set to 1000 kg.m^{-3}, 4200 J.(kg.°C)$^{-1}$, and 6×10^{-4} W·(mm·°C)$^{-1}$ respectively.

2.3. PMI multiphysics modeling

The multiphysics software was developed in our lab for the forward modeling of PMI and is performed in two steps. Firstly, propagation of light in the medium (Ω) is modeled using the diffusion equation [46–48]. Eq. 2. Technically, this step calculates the density of photons $\Phi(r)[\text{W mm}^{-2}]$ at any position r [mm] using the spatial distribution $\mu_a[\text{mm}^{-1}]$, and D [mm] of the absorption and diffusion coefficients, respectively. The diffusion coefficient D is defined as $D(r) = 1/3(\mu_a + \mu_s^{'})$ with $\mu_s^{'}[\text{mm}^{-1}]$ being the reduced scattering coefficient.

$$\begin{cases} -\nabla D(r)\nabla\Phi(r) + \mu_a(r)\Phi(r) = q_0(r) \\ \overrightarrow{n}\, D\nabla\Phi(r) + A\Phi(r) = 0 \quad (r \in \delta\Omega) \end{cases} \tag{2}$$

where $q_0(r)$ is the isotropic source of light, $\partial\Omega$ is the surface boundary, $\overrightarrow{n}$ is the vector normal to $\partial\Omega$, and A is the coefficient modeling the surface mismatch [49].

Secondly, the laser-induced increase in temperature T [°C] and its dynamics $T(r, t)$ within the medium are modeled using the Pennes bioheat equation [50]:

$$\begin{cases} \rho c\dfrac{\partial T(r,t)}{\partial t} - \nabla k\nabla T(r,t) = \Phi(r)\mu_a(r) \\ -k\dfrac{\partial T(r)}{\partial n} = h\left[T_f(r) - T(r)\right] \quad (r \in \delta\Omega) \end{cases} \tag{3}$$

where ρ $[\text{g mm}^{-3}]$ is the density, c $[\text{J}\ (\text{g}\ {}^\circ\text{C})^{-1}]$ the specific heat, and k $[\text{W}\ (\text{mm}\ {}^\circ\text{C})^{-1}]$ the thermal conductivity of the medium. The source of heat resulting from the laser light absorption by the medium is modeled by the product of the optical absorption and the photon density at any point within the medium [51,52]. T_f $[{}^\circ\text{C}]$ is the ambient temperature, and h $[\text{W}\ (\text{mm}^2 {}^\circ\text{C})^{-1}]$ is the heat transfer coefficient at the surface of the medium.

Once the PMI measurements are completed, the absorption coefficient of the medium under investigation can be estimated by minimizing the quadratic error between the measured MRT temperature and the simulated temperature maps from the forward solver. Here, the inverse problem is solved by iteratively minimizing the following objective function:

$$\Omega(\mu_a) = arg\ \min[T^m - T(\mu_a)] \tag{4}$$

T^m is the measured MRT temperature maps. While T is the simulated temperature map calculated by the forward solver for estimated overall μ_a [52,53].

3. Results and discussion

3.1. Homogeneous phantom results

At the beginning of the experiments, power for each laser is measured and recorded for calibration purposes. First, PMI is performed on both homogeneous phantoms, the one constructed with only Indian Ink (Horn Dye) and a combination of Indian Ink and AuNP nanorods (Horn AuNP). The phantoms are placed in the RF-coil, and temperature maps are acquired in a dynamic fashion for each wavelength one by one. Since the position of the source fiber that belongs to each wavelength differs slightly in the bundle, the illumination spot on the phantom also varies a little. To compensate for the change in the location, the first step in our multiphysics solver is an algorithm that estimates the position of the illumination spot from the MRT temperature maps.

Once the center and width of the spot are identified, a minimization algorithm is run to estimate the overall absorption coefficient of the phantom for each wavelength. Full dynamic data, acquired over 5.5 min (50 frames) that includes baseline, heating, and cooling frames, is utilized for this purpose. For homogeneous Dye phantom, the number of baseline, heating, and cooling frames are five, five, and forty, respectively. Fig. 5 shows sample data acquired with the homogeneous Dye and AuNP phantoms for a point just below the surface, where the peak temperature increase is achieved. Please note that mean baseline temperature maps acquired at the beginning of each data set (i.e. for each wavelength) are subtracted from the whole series to obtain the relative temperature increase for each point in the map.

The second step in the data analysis is to minimize the difference between the measured MRT map and the synthetic temperature map obtained by the multiphysics solver to estimate the overall absorption of the phantom for each wavelength one by one. Fig. 6 shows the measured MRT and the simulated temperature maps that belong to the 3rd heating frame for the homogeneous Dye phantom for each wavelength. The figure shows that the temperature elevation for 980 nm is three times the other four wavelengths due to high water absorption (0.0645 mm^{-1}). To compare the maps, profiles along the y-axis, from the top to the bottom of the phantom (indicated by a white dashed arrow), are plotted for each wavelength in the last row of Fig. 6. The profiles show a good agreement between the measured and simulated temperature maps above noise level of MRT. Using the data that belongs to all five wavelengths, the minimization algorithm successfully estimated the concentration as 39.44 ± 0.32 ng/ml, with only 0.5 % error in overall mean value.

The very same analysis is also performed for the AuNP homogeneous phantom. Fig. 7 depicts the recorded MRT and simulated temperature maps for the homogenous AuNP phantom, again for the 3rd heating frame for each wavelength. This time, the temperature elevation is higher for both 860 & 980 nm due to strong AuNP and water absorption, respectively. Profiles along the y-axis from top to bottom of the phantom (marked by a white dashed arrow) are shown for each wavelength in the last row of Fig. 7. Above the MRT noise level, the profiles demonstrate good agreement between the measured and simulated temperature maps. Again, the same minimization technique is used to estimate both Dye and AuNP concentration in the phantom. The Dye concentration is estimated as 39.99 ± 0.28 ng/ml, while the AuNP concentration is found to be 7.48 ± 0.07 mg/ml. These results correspond to an overall mean error of 0.9 % and 2.1 %, respectively. The high accuracy in the estimated concentration values is due to distinct differences in the absorption coefficients of Dye and AuNPs and the power of multi-wavelength measurements.

3.2 AuNP inclusion phantom results

Following the homogeneous phantom measurements, PMI is performed on the heterogeneous phantom with the AuNP inclusion. This time, the laser is turned on for 25 frames after five baseline images. Towards the end of the 25th heating frame, the maximum temperature elevation is around 10°C. At this point, the laser is turned off, and the imaging session ends since the agarose phantom starts showing signs of deformation. Fig. 8.a shows the schematic of the AuNP inclusion phantom. Dye concentration is the same everywhere, while the AuNPs are only confined inside the 8.8 mm diameter inclusion. The temperature map measured by the MRT at the 5th heating frame is presented in Fig. 8.b. The boundary of AuNP inclusion is represented by the white circle. As seen in this figure, the presence of the AuNPs in the inclusion actually allows heating that area but only the top part of the inclusion, as expected. If the AuNPs were not present, the inclusion temperature would be lower. To show their effect more clearly, the temperature map at that time point is simulated without the AuNPs and subtracted from the measured MRT map. This difference map demonstrates the temperature elevation due to AuNPs more clearly, Fig. 8.c.

For this experiment, the minimization process is performed using two compartments, the background and inclusion, whose boundary is delineated by the MRI. The algorithm estimates the concentration of the Dye and AuNPs in both compartments. The estimated values are very dose to the actual amounts. The Dye concentration is estimated as 39.87 ± 0.32 ng/ml in the background and 39.96 ± 0.35 ng/ml in the inclusion. AuNP concentration in the indusion is recovered as 7.44 ± 0.08 mg/ml. Fig. 9 demonstrates the measured and simulated temperature values for two distinct points selected in the AuNP indusion, indicated by S1& S2 in Fig. 8.a. They show an excellent agreement for the overall duration of the heating phase that continues for 25 frames (~165 s).

This experiment demonstrates that once the Dye and AuNP concentrations are appraised, the temperature elevation can be estimated at any point in the AuNP indusion using our multiphysics solver based on the known laser power and illumination time. Furthermore, temperature elevation can be calculated for a higher laser power or longer illumination durations. To demonstrate this ability of our multiphysics solver, laser power is tripled, and the temperature increase at the same points (SI & S2) is plotted in Fig. 9. As expected, the temperature at these points increased much higher, up to 30 °C and 8 °C for points SI and S2, respectively.

These results demonstrated that PMI has great potential to guide PTT successfully. Notably, it can provide AuNP concentration in tumors that will go under treatment and allow PTT preplanning. The efficacy of PTT is determined by the accuracy and performance of the heat delivery mechanism. As a result, it is critical to adjust experimental factors that regulate temperature elevation, such as laser power settings and exposure time. Determining these factors is crucial in order to avoid overheating during hyperthermia and underheating during thermolysis. As a result, during simulation studies, a specific thermal protocol should be devised to achieve these values prior to treatment of cancer with PTT, such as liver and breast cancer [54,55]. PMI can help this goal by providing the concentration of PTAs. In this study, we used our own Matlab-based multiphysics solver for this purpose, but a variety of advanced simulation tools are available in the literature. We use agarose phantoms to demonstrate the potential of PMI. This limits our experiments since the water starts to evaporate quickly when temperature elevation exceeds 8 °C, and the shape of the phantom starts to deform. However, agarose provides a suitable platform for making multi-compartment phantoms and including AuNPs in desired amounts.

To have the capability to perform measurements with five wavelengths to differentiate AuNPs successfully, we expand our PMI system in this study. The gold nanorods used for the experiments have a peak absorption around 850 nm. By changing their aspect ratios (length-to-width ratio), the peak absorption of gold nanorods can be timed. Moreover, there are different types of gold nanoparticles, such as spherical, hollow, and star-shaped ones, with various absorption spectra. Furthermore, besides inorganic PTAs such as AuNPs, carbon and iron-oxide particles, organic dyes, and polymer-based nanoparticles have also been utilized for PTT [56]. Due to its modular nature, expanding our PMI system by adding more lasers with different wavelengths is straightforward. Hence, our system can be tailored for other PTAs with different absorption spectra. The critical wavelength range for deep tissue imaging is the near-infrared band since the total optical absorption of the endogenous tissue absorbers, such as oxy- and deoxy-hemoglobin, water, and fat, is minimal. Hence, the wavelengths of the PMI system described in this study can be tailored to any PTA that has a peak absorption in the near-infrared region since their absorption spectrum is distinctly different than the tissue endogenous absorbers.

Another novelty of this approach comes from the fact that if multiple exogenous agents are utilized (i.e. multiple AuNPs and/or Indocyanine Green), more wavelengths can be added to resolve each exogenous agent separately. For example, AuNPs can be tailored to target the tumor, while Indocyanine Green can be utilized simultaneously to measure tumor perfusion. Finally, by leveraging the sensitivity of the optical molecular imaging and resolution of the MRI, PMI can a perfect alternative for imaging of AuNPs compared to the other available techniques. Anatomic imaging modalities like X-ray CT in fluorescence mode [15, 16]. or MRI with superparamagnetic materials has been utilized earlier [21]. Unfortunately, their sensitivity is low.

Meanwhile, more sensitive techniques like fluorescence molecular tomography suffered from low resolution. An alternative high-resolution technique, Photoacoustic imaging, requires ultrasound detectors to contact the tissue and offers dept-dependent resolution. Being non-contact and providing relatively dept-independent resolution are the strengths of the PMI. MRI is readily used as a monitoring tool for PTT; therefore, PMI will be a natural addition to this platform, another main advantage compared to the other imaging modalities.

4. Conclusion

Among all available PTAs, AuNPs have gained special attention due to their biocompatible and plasmonic properties, adjustable photothermal conversion efficiency parameters, imaging potential, and high surface loading ability of drugs. Their primary advantage is to increase the selective thermal damage during PTT. Multi-wavelength PMI can be used to determine the amount of AuNPs accumulated in the tumor, which is necessary to facilitate accurate simulations to determine the optimum PTT parameters, such as laser illumination power, duration, wavelength, and spot size. There is a great interest in building computational tools to simulate the PTT results utilizing different AuNP distribution amounts and patterns [57]. Multi-wavelength PMI is a perfect candidate to guide PTT as these new computational studies demonstrate the importance of estimating AuNP concentration in tumors prior to the therapy.

Acknowledgments

The authors would like to thank Mohamed I. Abdelwahab for his participation in data generation. This research is supported in part by NIH grants, F31CA171915-01A1, SBIRHHSN261201300068C, 1R21CA191389, R21EB013387, R01EB008716, UCI Cancer Center P30CA062203, Mohammad Ibn Saud Islamic University.

Data availability

The data used in this study is available upon request from the corresponding author.

References

[1]. Cheng Y, Weng S, Yu L, Zhu N, Yang M, Yuan Y, The role of hyperthermia in the multidisciplinary treatment of malignant tumors, Integr. Cancer Ther. 18 (2019) 1534735419876345.

[2]. Issels RD, Lindner LH, Verweij J, Wust P, Reichardt P, Schem BC, Abdel-Rahman S, Daugaard S, Salat C, Wendtner CM, Vujaskovic Z, Wessalowski R, Jauch KW, Dürr HR, Ploner F, Baur-Melnyk A, Mansmann U, Hiddemann W, Blay JY, Hohenberger P, E.O.f.R.aT.o.C.S.T.a.B.S.G. (EORTC-STBSG), E.S.f.H.O. (ESHO), Neo-adjuvant chemotherapy alone or with regional hyperthermia for localised high-risk soft-tissue sarcoma: a randomised phase 3 multicentre study, Lancet Oncol. 11 (6) (2010) 561–570. [PubMed: 20434400]

[3]. Moon HK, Lee SH, Choi HC, In vivo near-infrared mediated tumor destruction by photothermal effect of carbon nanotubes, ACS Nano 3 (11) (2009) 3707–3713. [PubMed: 19877694]

[4]. Zhao L, Zhang X, Wang X, Guan X, Zhang W, Ma J, Recent advances in selective photothermal therapy of tumor, J. Nanobiotechnol 19 (1) (2021) 335.

[5]. Vankayala R, Huang YK, Kalluru P, Chiang CS, Hwang KC, First demonstration of gold nanorods-mediated photodynamic therapeutic destruction of tumors via near infra-red light activation, Small 10 (8) (2014) 1612–1622. [PubMed: 24339243]

[6]. Depciuch J, Stec M, Maximienko A, Baran J, Parlinska-Wojtan M, Size-dependent theoretical and experimental photothermal conversion efficiency of spherical gold nanoparticles, Photodiagnosis Photodyn. Ther 39 (2022) 102979.

[7]. Singh AK, Srivastava ON, One-step green synthesis of gold nanoparticles using black cardamom and effect of pH on its synthesis, Nanoscale Res. Lett 10 (1) 1055.

[8]. Yang W, Xia B, Wang L, Ma S, Liang H, Wang D, Huang J, Shape effects of gold nanoparticles in photothermal cancer therapy, Mater. Today Sustain 13 (2021).

[9]. Chithrani BD, Ghazani AA, Chan WC, Determining the size and shape dependence of gold nanoparticle uptake into mammalian cells, Nano Lett. 6 (4) (2006) 662–668. [PubMed: 16608261]

[10]. Engstrom AM, Faase RA, Marquart GW, Baio JE, Mackiewicz MR, Harper SL, Size-dependent interactions of lipid-coated gold nanoparticles: developing a better mechanistic understanding through model cell membranes and in vivo toxicity, Int. J. Nanomed 15 (2020) 4091–4104.

[11]. Wang B, Wang JH, Liu Q, Huang H, Chen M, Li K, Li C, Yu XF, Chu PK, Rose-bengal-conjugated gold nanorods for in vivo photodynamic and photothermal oral cancer therapies, BiomaterialsBiomaterials 35 (6) (2014) 1954–1966.

[12]. Vankayala R, Lin CC, Kalluru P, Chiang CS, Hwang KC, Gold nanoshells-mediated bimodal photodynamic and photothermal cancer treatment using ultra-low doses of near infra-red light, BiomaterialsBiomaterials 35 (21) (2014) 5527–5538.

[13]. Ali AA, Abuwatfa WH, Al-Sayah MH, Husseini GA, Gold-nanoparticle hybrid nanostructures for multimodal cancer therapy, Nanomaterials (Basel) 12 (20) (2022).

[14]. Alamzadeh Z, Beik J, Mirrahimi M, Shakeri-Zadeh A, Ebrahimi F, Komeili A, Ghalandari H. Ghaznavi, S.K. Kamrava, C. Moustakis, Gold nanoparticles promote a multimodal synergistic cancer therapy strategy by co-delivery of thermo-chemo-radio therapy, Eur. J. Pharm. Sci 145 (2020) 105235.

[15]. Manohar N, Reynoso FJ, Diagaradjane P, Krishnan S, Cho SH, Quantitative imaging of gold nanoparticle distribution in a tumor-bearing mouse using benchtop X-ray fluorescence computed tomography, Sci. Rep 6 (2016) 22079. [PubMed: 26912068]

[16]. Zhang S, Li L, Chen J, Chen Z, Zhang W, Lu H, Quantitative imaging of Gd nanoparticles in mice using benchtop cone-beam X-ray fluorescence computed tomography system, Int. J. Mol. Sd 20 (9) (2019).

[17]. Staufer T, Grüner F, Review of development and recent advances in biomedical X-ray fluorescence imaging, Int. J. Mol. Sci 24 (13) (2023).

[18]. Kim T, Lee WS, Jeon M, Kim H, Eom M, Jung S, Im HJ, Ye SJ, Dual imaging modality of fluorescence and transmission X-rays for gold nanoparticle-injected living mice, Med. Phys 50 (1) (2023) 529–539. [PubMed: 36367111]

[19]. Kim J, Park S, Lee JE, Jin SM, Lee JH, Lee IS, Yang I, Kim JS, Kim SK, Cho MH, Hyeon T, Designed fabrication of multifunctional magnetic gold nanoshells and their application to magnetic resonance imaging and photothermal therapy, Angew. Chem. Int. Ed Engl 45 (46) (2006) 7754–7758. [PubMed: 17072921]

[20]. Debouttiere P, Roux S, Vocanson F, Billotey C, Beuf O, Favre-Reguillon A, Lin Y, Pellet-Rostaing S, Lamartine R, Perriat P, Tillement O, Design of gold nanoparticles for magnetic resonance imaging, Adv. Funct. Mater 16 (18) (2006) 2330–2339.

[21]. Sanchez A, Paredes K, Ruiz-Cabello J, Martinez-Ruiz P, Pingarron J, Villalonga R, Filice M, Hybrid decorated core@shell janus nanoparticles as a flexible platform for targeted multimodal molecular bioimaging of cancer, ACS AppL Mater. Interfaces 10 (37) (2018) 31032–31043. [PubMed: 30141615]

[22]. Bouché M, Hsu JC, Dong YC, Kim J, Taing K, Cormode DP, Recent advances in molecular imaging with gold nanoparticles, Bioconjug. Chem 31 (2) (2020) 303–314. [PubMed: 31682405]

[23]. Harmsen S, Huang R, A Wall M, Karabeber H, Samii JM, Spaliviero M, White JR, Monette S, O’Connor R, Pitter KL, Sastra SA, Saborowski M, Holland E, Singer S, Olive KP, Lowe SW, Blasberg RG, Kircher MF, Surface-enhanced resonance Raman scattering nanostars for high-precision cancer imaging, Sd. Transi. Med 7 (271) (2015) 271ra7

[24]. Liba O, SoRelle ED, Sen D, A de la Zerda, Contrast-enhanced optical coherence tomography with picomolar sensitivity for functional in vivo imaging, Sci. Rep 6 23337.

[25]. Swierczewska M, Lee S, Chen X, The design and application of fluorophore-gold nanopartide activatable probes, Phys. Chem. Chem. Phys 13 (21) (2011) 9929–9941. [PubMed: 21380462]

[26]. Kong Y, Chen J, Gao F, Brydson R, Johnson B, Heath G, Zhang Y, Wu L, Zhou, Near-infrared fluorescent ribonudease-A-encapsulated gold nanodusters: preparation, characterization, cancer targeting and imaging, Nanoscale 5 (3) (2013) 1009–1017. [PubMed: 23249999]

[27]. Zhou C, Long M, Qin Y, Sun X, Zheng J, Luminescent gold nanoparticles with efficient renal clearance, Angew. Chem. Int. Ed Engl 50 (14) (2011) 3168–3172. [PubMed: 21374769]

[28]. Song X, Zhu W, Ge X, Li R, Li S, Chen X, Song J, Xie J, Yang H, A new dass of NIR-n gold nanoduster-based protein biolabels for in vivo tumor-targeted imaging, Angew. Chem. Int. Ed Engl 60 (3) (2021) 1306–1312. [PubMed: 32940954]

[29]. Gamelin J MAAAHFGPWLV, Zhu Q, A real-time photoacoustic tomography system for small animals, Opt. Express 17 (13) (2009) 10489. [PubMed: 19550444]

[30]. Stein EW, Maslov K, Wang LV, Noninvasive, in vivo imaging of blood-oxygenation dynamics within the mouse brain using photoacoustic microscopy, J. Biomed. Opt 14 (2) (2009) 020502.

[31]. Liu Y, Bhattarai P, Dai Z, Chen X, Photothermal therapy and photoacoustic imaging via nanotheranostics in fighting cancer, Chem. Soc. Rev 48 (7) (2019) 2053–2108. [PubMed: 30259015]

[32]. Li W, Chen X, Gold nanopartides for photoacoustic imaging, Nanomedicine (Lond) 10 (2) (2015) 299–320. [PubMed: 25600972]

[33]. Lin DTY, Gulsen G, Laser-induced photomagnetic imaging, Appl. Phys. Lett, press (2012).

[34]. Luk A, Nouizi F, Erkol H, Unlu MB, Gulsen G, Ex vivo validation of photo-magnetic imaging, Opt. Lett 42 (20) (2017) 4171–4174. [PubMed: 29028040]

[35]. Algarawi M, Erkol H, Luk A, Ha S, Burdn Unlu M, Gulsen G, Nouizi F, Multi-wavelength photo-magnetic imaging system for photothermal therapy guidance, Lasers Suig. Med 53 (5) (2021) 713–721.

[36]. van Veen RL, Sterenborg HJ, Pifferi A, Torricelli A, Chikoidze E, Cubeddu R, Determination of visible near-IR absorption coeffidents of mammalian fot using time- and spatially resolved diffuse reflectance and transmission spectroscopy, J. Biomed. Opt 10 (5) (2005) 054004.

[37]. Kukreti S, Cerussi AE, Tanamai W, Hsiang D, Tromberg BJ, Gratton E, Characterization of metabolic differences between benign and malignant tumors: high-spectral-resolution diffuse optical spectroscopy, RadiologyRadiology 254(1) 277–284.

[38]. Meng X, Zhang B, Yi Y, Cheng H, Wang B, Liu Y, Gong T, Yang W, Yao Y, Wang H, Bu W, Accurate and real-time temperature monitoring during MR imaging guided PTT, Nano Lett. 20 (4) (2020) 2522–2529. [PubMed: 32208714]

[39]. West CL, Doughty ACV, Liu K, Chen WR, Monitoring tissue temperature during photothermal therapy for cancer, J. BioX Res 2 (4) (2019) 159–168. [PubMed: 33088609]

[40]. McDannold N, Quantitative MRI-based temperature mapping based on the proton resonant frequency shift: review of validation studies, Int. J. Hyperthermia 21 (6) (2005) 533–546. [PubMed: 16147438]

[41]. Lualdi M, Colombo A, Farina B, Tomatis S, Marchesini R, A phantom with tissue-like optical properties in the visible and near infrared for use in photomedicine, Lasers Surg. Med 28 (3) (2001) 237–243. [PubMed: 11295758]

[42]. Li D, Meaney PM, Tosteson TD, Jiang S, Kerner TE, McBride TO, Pogue BW, Hartov A, Paulsen KD, Comparisons of three alternative breast modalities in a common phantom imaging experiment, Med. Phys 30 (8) (2003) 2194–2205. [PubMed: 12945985]

[43]. Y Lin DT, Naldoglu O, Gulsen G, Tumor characterization in small animals using MR-guided dynamic contrast enhanced diffuse optical tomography (DCE-DOT), J. Biomed. Opt (2011). In press.

[44]. Lin Y, Gao H, Nalcioglu O, Gulsen G, Fluorescence diffuse optical tomography with functional and anatomical a priori information: feasibility study, Phys. Med. Biol 52 (18) (2007) 5569–5585. [PubMed: 17804882]

[45]. Gulsen G UMB, Birgul O, Shafiiha R, Nalcioglu O, Combined diffuse optical tomography (DOT) and MRI system for cancer imaging in small animals, Technol. Cancer Res. Treat 5 (2006) 351–364. [PubMed: 16866566]

[46]. Arridge S, Photon-measurement density functions. Part I: analytical forms, AppL Opt. 34 (1999) 7395–7409.

[47]. Schweiger M, Arridge SR, Hiraoka M, Delpy DT, The finite element method for the propagation of light in scattering media: boundary and source conditions, Med. Phys 22 (11 Pt 1) (1995) 1779–1792. [PubMed: 8587533]

[48]. Hebden J, Arridge S, Delpy D, Optical imaging in medicine. I. Experimental techniques, Phys. Med. Biol 42 (1997) 825–840. [PubMed: 9172262]

[49]. Nouizi F, Torregrossa M, Chabrier R, Poulet P, Improvement of absorption and scattering discrimination by selection of sensitive points on temporal profile in diffuse optical tomography, Opt. Express 19 (13) (2011) 12843–12854. [PubMed: 21716527]

[50]. Wissler EH, Pennes' 1948 paper revisited, J. Appl. Physiol 85 (1) (1998) 35–41 (1985). [PubMed: 9655751]

[51]. Diaz SH, Aguilar G, Lavemia EJ, Wong BJF, Modeling the thermal response of porcine cartilage to laser irradiation, IEEE, Selected Topics Quant. Electron (2001) 944–951.

[52]. Lin Y, Gao H, Thayer D, Luk AL, Gulsen G, Photo-magnetic imaging: resolving optical contrast at MRI resolution, Phys. Med. Biol 58 (11) (2013) 3551–3562. [PubMed: 23640084]

[53]. Nouizi F, Luk A, Thayer D, Lin Y, Ha S, Gulsen G, Experimental validation of a high-resolution diffuse optical imaging modality: photomagnetic imaging, J. Biomed. Opt 21 (1) (2016) 16009.

[54]. Taghizadeh S, Alimardani V, Roudbali PL, Ghasemi Y, Kaviani E, Gold nanopartides application in liver cancer, Photodiagnosis Photodyn. Ther 25 (2019) 389–400. [PubMed: 30684673]

[55]. Mohseni H, Imanparast A, Salarabadi SS, Sazgamia A, In vitro evaluation of the intensifying photodynamic effect due to the presence of plasmonic hollow gold nanoshells loaded with methylene blue on breast and melanoma cancer cells, Photodiagnosis Photodyn. Ther 40 (2022) 103065.

[56]. Lv S, Miao Y, Liu D, Song F, Recent development of photothermal agents (ptas) based on small organic molecular dyes, ChemBioChem 21 (15) (2020) 2098–2110. [PubMed: 32202062]

[57]. Cheong JK, Ooi EH, Chiew YS, Menichetti L, Armanetti P, Franchini MC, Alchera E, Locatelli I, Canu T, Maturi M, Popov V, Alfano M, Gold nanorods assisted photothermal therapy of bladder cancer in mice: a computational study on the effects of gold nanorods distribution at the centre, periphery, and surface of bladder cancer, Comput. Methods Programs Biomed 230 (2023) 107363.

Fig. 1.

The PMI system consists of: a) the main unit that has the high-power lasers and their drivers, a temperature management system, and a control computer, b) the optical fiber bundle coupled RF-coil for MR temperature imaging with laser light illumination.

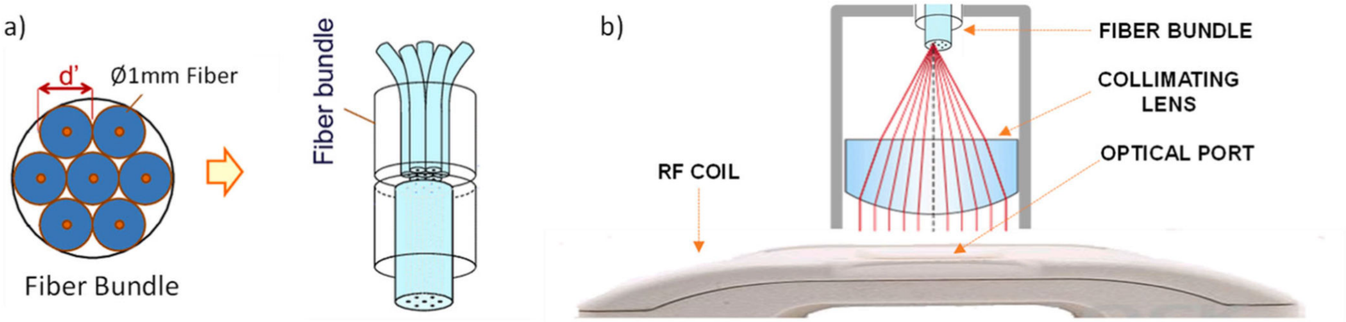

Fig. 2.

a) The fiber bundle is custom built in our lab and has seven Ø1 mm fibers that transfer light from the laser outputs to the RF-coil. b) The light output of the bundle is collimated using an aspheric lens and directed to the surface of the phantom using an opening at the top of the RF-coil.

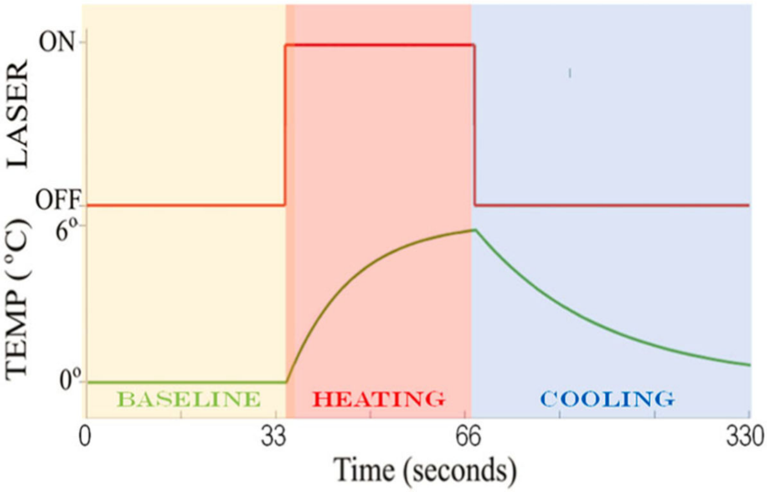

Fig. 3.

a) During PMI, baseline MRT images are acquired while the laser is off. Following that, the laser is turned on while the MRT continues to acquire images of the laser-induced temperature elevation. The final stage of the PMI data acquisition is the cooling phase, when the laser is turned off, and MRT images are acquired while the medium under investigation cools down.

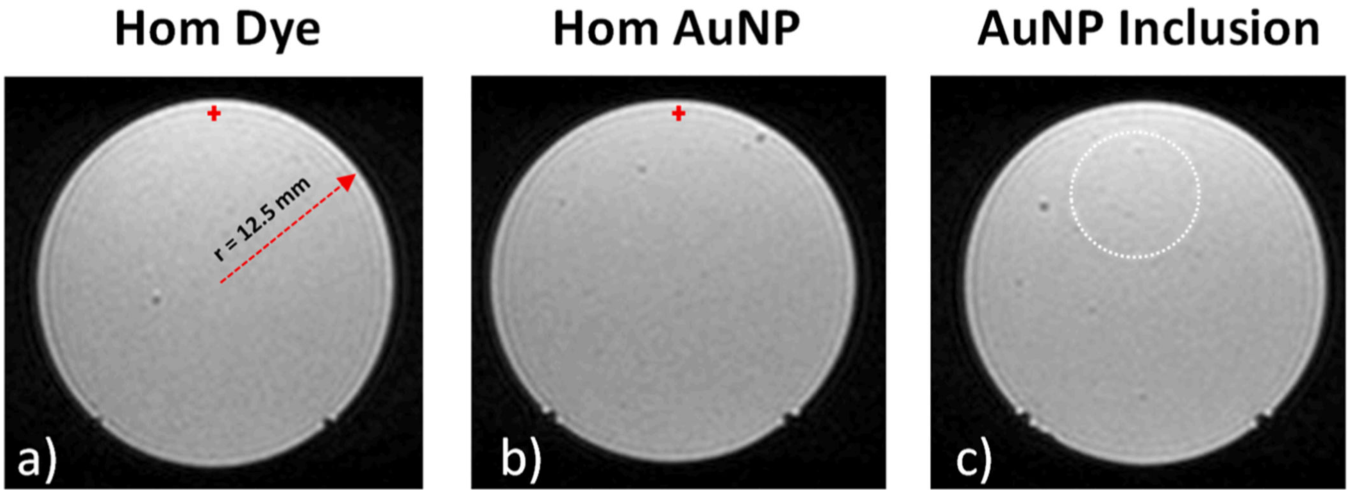

Fig. 4.

T1-weighted MR image representing a cross-section of the 25-mm-diameter phantoms: a) the homogeneous Dye, b) the homogeneous AuNPs, and c) the AuNP inclusion phantom. The boundary of the inclusion is represented by the white dashed circle, while the red plus signs show the approximate position for which the temperature profiles are presented in Fig. 5).

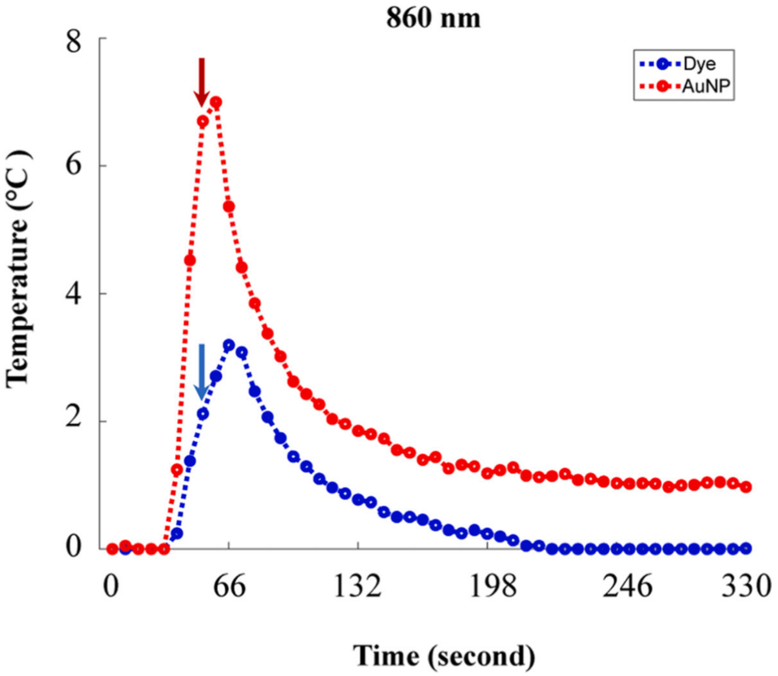

Fig. 5.

Temporal profiles for the homogeneous Dye and homogeneous AuNP phantoms, for the points represented with red plus signs in Fig. 4. As expected, the temperature elevation is much higher in the AuNP phantom, since its absorption is much higher compare to the Dye phantom at 860 nm, Table 1. The blue and red arrow indicates the 3rd heating frame for both phantoms, for which the temperature maps are given in Figs. 6& 7.

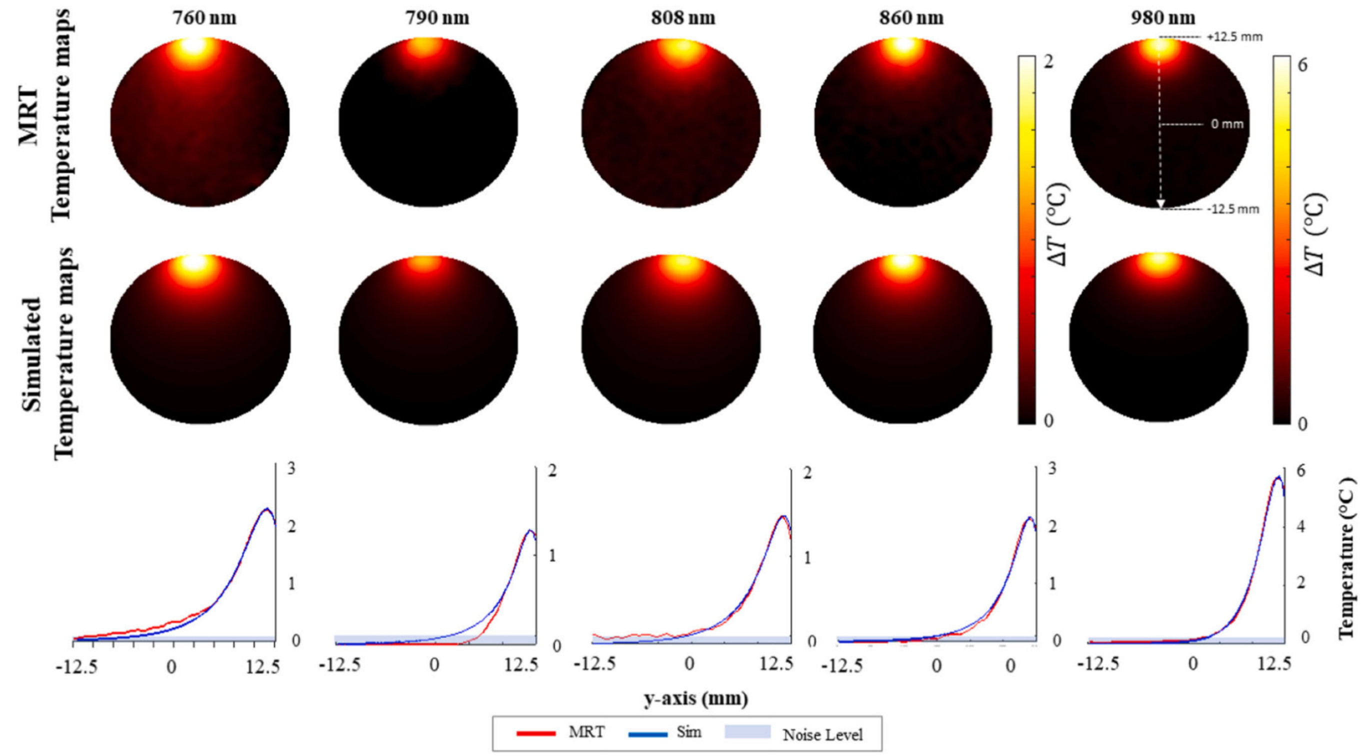

Fig. 6.

The measured MRT and simulated temperature maps using our multiphysics solver for the homogeneous Dye phantom are shown in the first and second rows, respectively. The maps that belong to a distinct wavelength are presented in each column. Since the temperature elevation for 980 nm is much higher, a different colorbar is used for the last column. The third row shows the profiles along the dashed line represented in 980 nm MRT map, for both measured (red) and simulated (blue) temperature maps. They show a very good agreement above the MRT noise level highlighted with blue.

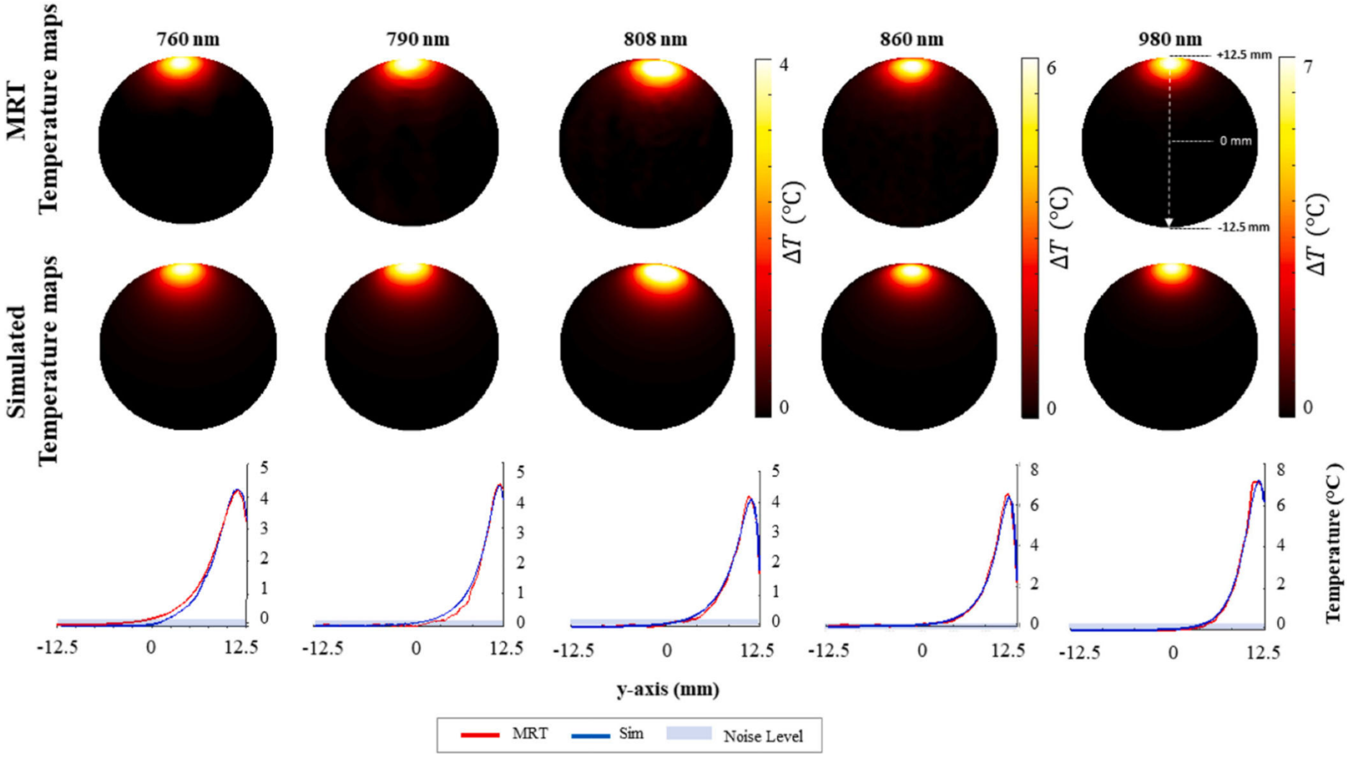

Fig. 7.

The measured MRT and simulated temperature maps using our multiphysics solver for the homogeneous AuNP phantom are shown in the first and second rows. The maps that belong to a distinct wavelength are presented in each column. Since the temperature elevation for 860 and 980 nm is much higher, different colorbars are used for the last two columns. The third row shows the profiles along the dashed line represented in 980 nm MRT map. There is a very good agreement between measured (red) and simulated (blue) temperature maps above the MRT noise level highlighted with blue.

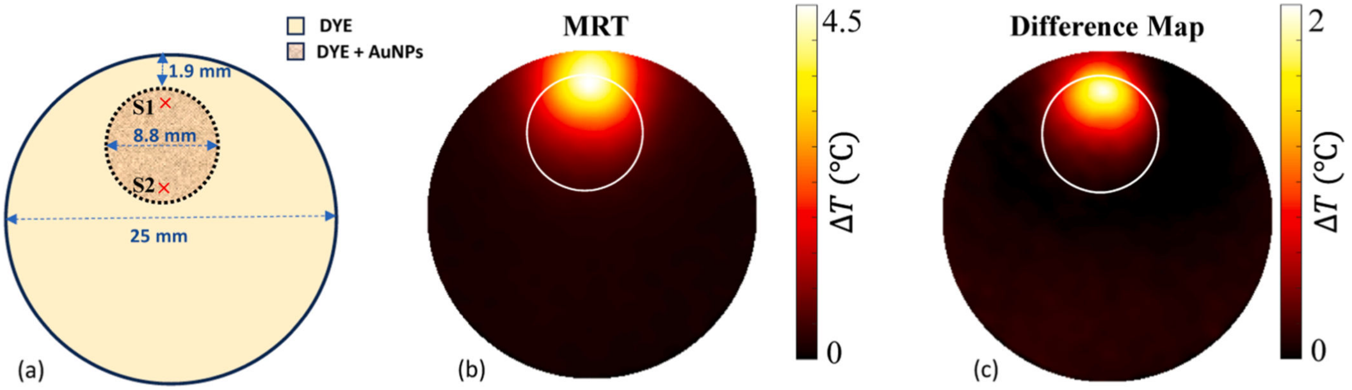

Fig. 8.

a) Schematic of the AuNP inclusion phantom. Two distinct points are selected in the AuNP inclusion for analysis of the temporal evolution of temperature, indicated by S1& S2. b) The measured MRT temperature map at the 5th heating frame, c) To show the effect of the AuNPs, the simulated temperature map without their presence is subtracted from the MRT map.

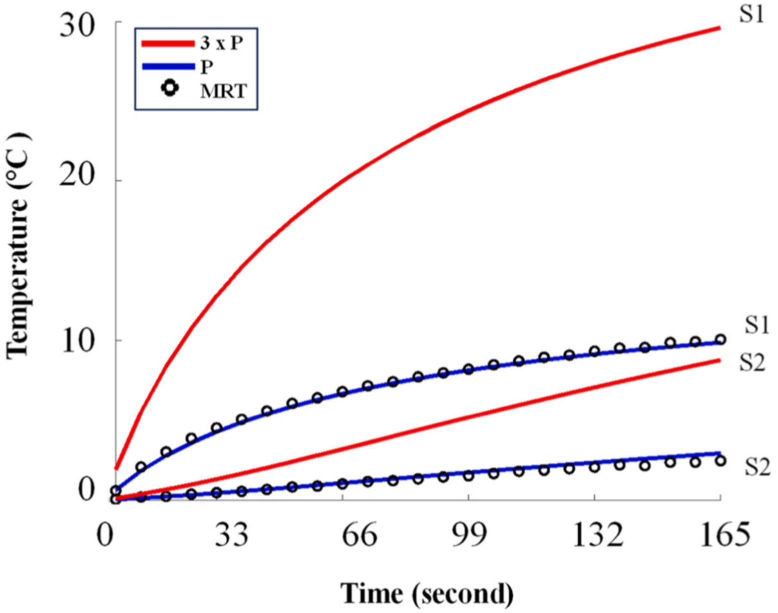

Fig. 9.

The measured (black circles) and simulated (blue solid line) temperature values for two distinct points selected in the AuNP inclusion, S1 & S2. To show the capability of estimating the evolution of temperature at these points with higher laser power, simulations are performed. The laser power is increased three-fold, and the temporal evolution of the temperature at the same points (S1 & S2) is plotted with a solid red line. As expected, the temperature increases much more when higher laser power is utilized.

Table 1

The absorption coefficient ($\mu a \ [mm^{-1}]$) of the individual components together with the total absorption coefficients of homogeneous Dye (Hom Dye) & AuNP (Hom AuNP) phantoms.

	760 nm	**790 nm**	**808 nm**	**860 nm**	**980 nm**
Indian Ink (39.6 ng/ml)	0.0101	0.0098	0.0097	0.0090	0.0129
AuNPs (7.33 μg/ml)	0.0115	0.0201	0.0241	0.0267	0.0122
Fat & water	0.0039	0.0025	0.0025	0.0049	0.0516
Hom Dye Phantom	0.0141	0.0123	0.0122	0.0140	0.0645
Hom AuNP Phantom	0.0255	0.0324	0.0363	0.0407	0.0761